



## Research Article

# Fabrication of Ni–Al composite coating on stainless steel using hybrid gas-phase coating technique and its corrosion study

Amin D. Thamir<sup>1</sup> · Faras Q. Mohammed<sup>2</sup> · Mahdie Mutier Hanon<sup>1</sup>

© Springer Nature Switzerland AG 2019

## Abstract

Working in high-concentration acidic environments is required in some important applications. One of the most important determinants of using stainless steel is the breakage when working at high acidic concentrations, where failure can occur by a mechanism similar to chloride attack that leads to stress corrosion cracking. On the other hand, superalloys containing nickel are chosen to be used in certain applications because of their good surface stability, corrosion resistance, and oxidation resistance. In this work, a composite coating based on Ni–Al phases was performed by using a hybrid gas-phase coating technique on the surface of 316 austenitic stainless steels. The deposition temperatures were ranging from  $T_d=650\text{--}950\text{ }^\circ\text{C}$ , where the Ni–Al-based vapors was obtained in an evacuated chamber by using pure metal powders in such system. The structural characterization for the deposited Ni–Al coating was performed by using XRD technique and the scanning electron microscopy. The scratch test was performed to determine the thin-film adhesion with the substrate by a diamond indenter that was drawn across the coated surface under a specific load. Electrochemical corrosion tests have been performed to obtain the anodic polarization curves for the base metal and the coated surfaces. From the electrochemical test, the Ni–Al coating surfaces show a great future in reducing the current density of the steel surface in the anodic region, which indicating improved pitting resistance for all Ni–Al coating samples. No pitting corrosion was observed after the test in all the coated surfaces were deposited at 750, 850, and 950 °C with Inters. Pot.: –495.1 (mV) Inters. Cur.: 18.35  $\mu\text{A}$ , Inters. Pot.: –661.5 (mV) Inters. Cur.: 11.94  $\mu\text{A}$ , and Inters. Pot.: –344.4 (mV) Inters. Cur.: 7.19  $\mu\text{A}$ , respectively, at potential test that reaches up to 2000 mV (i.e., no breakdown potential).

**Keywords** AISI316 · Ni–Al coatings · Pitting corrosion · Hybrid gas phase · Breakdown potential

## 1 Introduction

Austenitic stainless steels constitute the largest stainless family that is widely used in various sectors of the industry. Type 316 of austenitic stainless steel has the broadest range of usefulness for storage vessels, pumps, and process equipment handling glacial acetic acid, which would be discolored by type 304 [1]. Most stainless steels, including austenitic and duplex grades, are known to be susceptible to cracking when used in high-concentration acid environment, probably by a mechanism similar to chloride

attack by stress corrosion cracking (SCC). Thus, the austenitic stainless steels such as type 316 of stainless steel are not generally recommended for storing the hydrochloric acid in petroleum planets, except when solutions are very diluted at room temperature, otherwise pitting may occur [2]. Pitting corrosion is a localized electrochemical dissolution process that in some cases can cause a catastrophic failure of passive metals such as the austenitic stainless steels. The initial event in localized corrosion of stainless steels is passivity breakdown, followed by nucleation and pit growth, where the stainless steels are rapidly attacked

✉ Faras Q. Mohammed, 11795@uotechnology.edu.iq; Amin D. Thamir, dr.amin@uotechnology.edu.iq; Mahdie Mutier Hanon, jawaddy@yahoo.com | <sup>1</sup>Department of Production Engineering and Metallurgy, University of Technology, Baghdad, Iraq. <sup>2</sup>Nanotechnology and Advanced Material Research Center, University of Technology, Baghdad, Iraq.



by strong HCl because a passive film is not easily attained [3]. To solve this problem, nickel-containing superalloys can be selected for using in certain applications due to their characteristics. Among their important characteristics are creep resistance at high temperatures, good surface stability, and corrosion and oxidation resistance. One of their most important properties is high-temperature creep resistance [1, 4]. Nickel-based superalloys are made age hardened by the introduction of aluminum and titanium into their alloy compositions; according to this, the melting temperature for the NiAl increases by approximately 300 °C higher than nickel-based superalloys (NiAl melts congruently at 2980 °F (1638 °C)). The major improvement in high-temperature strength, however, is the result of the precipitation of the intermetallic compound, Ni<sub>3</sub>(Al, Ti); it is usually called gamma prime [5, 6]. In some alloys, cobalt is used as a replacement for part of the nickel. NiAl has a wide single-phase field which extends from 45 to 60% at Ni and density of 0.21 lb/in<sup>3</sup> (5.9 g/cm<sup>3</sup> approximately 2/3 of nickel-based superalloys) [1, 7]. In this work, the deposition of the Ni–Al film on the stainless-steels substrate by gas-phase deposition process has been done by a new hybrid deposition technique [8]. In this technique, the coating materials supplied in the form of the gas phase were produced by evaporating a number of powders by using thermal energy (i.e., PVD thermal reactive evaporation), while the deposition path on the surface of the base metal is based on the CVD technique. The effect of the process parameters has also been determined; the most important of these effects on the formation of the thin film is nitrogen flow rates as well as the base metal deposition temperature.

## 2 Experimental work

Deposition experiments for the surface layer were carried out by using HDP equipment, where the Ni–Al-based vapors were produced in a vacuum chamber in such a

system. Details and features of this production facility are displayed in Fig. 1. The reaction temperature and flow rate of the carrier gas were carefully controlled. The components of the thin surface film were contained in an alumina boat by placing different powders in the center of the boat. The gas-phase deposition system that was used in this work consists of four units as shown below:

1. Powder evaporation unit.
2. Gas feed unit.
3. Deposition chamber.
4. Exhaust gas system.

Different metal powders were used in this work. A pure aluminum powder (Al) with purity of 95% Al was provided by Fisher Scientific (USA), with average particle size 5.841 μm. Also, a pure nickel powder (Ni) with purity 99.95% (Ni) was provided by High Media (India), with average particle size 25.93 μm. Nitrogen gas (supplied by Iraqi gas product factory with purity 99.999%) was used as a carrier gas. The NiAl deposition process was performed at different deposition temperatures (650, 750, 850 and 950 °C), and by using the same nitrogen flow rate at flow of 2.5SLPM (standard liter per minute). The experimental work, which was aimed at evaluating the microstructure and the surface morphology, was made by using austenitic stainless-steel AISI 316 as the substrate material in this work, where this steel chemical composition contains 0.020 wt% C, 17.13 wt% Cr, 11.19 wt% Ni, 0.49 wt% Si, 1.28 wt% Mn, 0.029 wt% P, 0.003 wt% S, 2.09 wt% Mo, 0.16 wt% Co, and 0.032 wt% N. The test samples were prepared according to different tests required for each sample. The samples for phase characterization (XRD) and structural morphology (SEM) have the dimensions of 2 × 5 × 10 mm for the thickness, height, and width, respectively. For the electrochemical tests, the specimens of 1 cm<sup>2</sup> surface area were used in this work. The constituents of the different phases were detected by using an X-ray diffractometer (XRD-6000X Shimadzu X-ray diffractometer with using

**Fig. 1** Mixed gas-phase deposition process system equipment



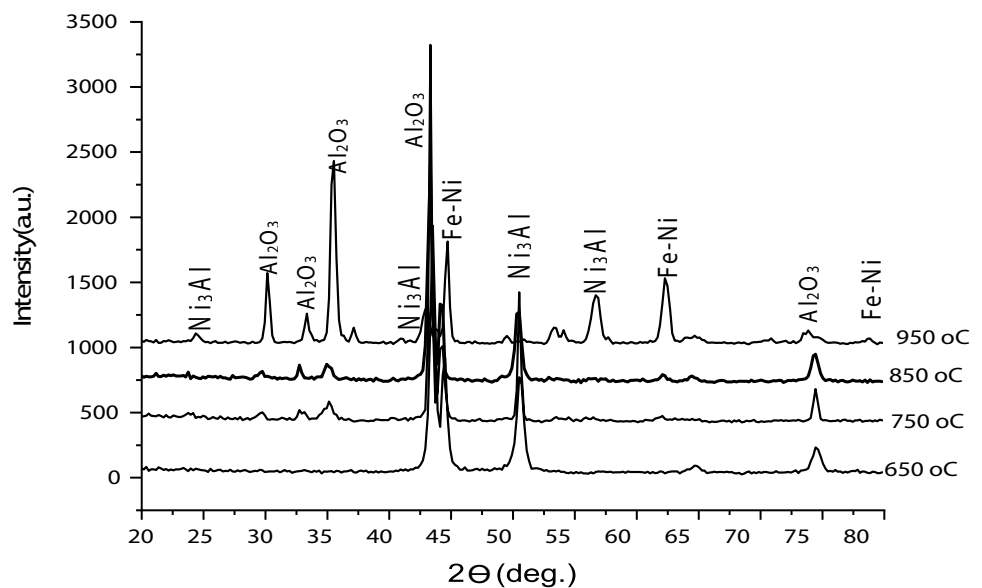
an incident angle of 0.154 nm with copper-K $\alpha$  radiation). For the topographical features of the upper surface of the Ni–Al coating, the TESCAN Vega 3SB electronic scanning microscope test was performed with a voltage acceleration of 200 V to 30 kV and a magnification force of  $6 \times$  to 100,000 $\times$ . The scratch test was performed by SHEEN 705 scratch tester (England) needle type, which was fitted with a Rockwell C diamond stylus (cone apex angle, 120 $^\circ$ , and 200  $\mu\text{m}$  tip radius) for a traverse length of 10 mm. The scratches were performed at a load of 30 N, and the surface of the specimens was cleaned ultrasonically before the test. The electrochemical corrosion tests have been performed by using a WIKING M-Labsci Potentiostat from Bank-Elektronik with computer data login, requisition, and analysis system. The specimen was clamped to the cell; 1.0 cm $^2$  of the specimen surface was exposed to the electrolyte. It was operated a Pt electrode as a counter electrode and a saturated calomel electrode (SCE) as a reference electrode. The electrolyte solution was designed to cause pitting corrosion by a high concentration of chlorides; the electrolyte that was used for the tests was 0.25 M hydrochloric acid (HCl) aqueous solution in deionized water. The anodic polarization curves were recorded with a sweep speed of 2 mVs $^{-1}$  at 22  $^\circ\text{C}$  to measure the anodic polarization curves of the uncoated and coated surfaces. The surface roughness of all samples was increased in order to improve the adhesion potential of the metal vapor on the surface of the sample; all samples were mechanically grinded on the emery sheet of grit 240 and then rinsed with acetone. Also, all samples were cleaned prior to the deposition process by ultrasonic cleaning in ethanol for 15 min prior to the deposition process.

## 3 Results and discussion

### 3.1 XRD results

In our study, it was very clear that the deposition rates and the produced coating phases in the coating film were affected by the deposition temperature. This was very clear since the coating film that was deposited at 650  $^\circ\text{C}$  does not contain any phases that were resulted from Al–Ni compounds as shown in Fig. 2. This figure shows the XRD pattern for Al–Ni coatings that were deposited at different deposition temperatures. In Fig. 2, at 650  $^\circ\text{C}$ , only Fe–Ni contains 93% Fe 6.29% Ni (centrosymmetric structure), and aluminum oxide ( $\text{Al}_2\text{O}_3$ ) compounds that contain 52.93% Al 47.07% O can be found in this pattern (ICDD no. 00-037-0474 and 00-010-0173, respectively). With higher deposition temperature, a change in the presented phases will result in. Also, a change can result in the deposition rate while increasing the deposition temperature as the coating film will be formed in the stable region of a phase diagram [8, 9]. At 750  $^\circ\text{C}$ , the increase in the deposition temperature results in a change in the presented phases, which can be driven by the higher deposition rate compared to the former coating film (at 650  $^\circ\text{C}$ ). The XRD pattern in Fig. 2 for the samples that were deposited at 750  $^\circ\text{C}$  shows higher peak intensity for Fe–Ni and  $\text{Al}_2\text{O}_3$  phases, in addition to peak broadening that was resulted from more crystalline structure and grain growth, which can be driven by the higher deposition temperature compared to the former coating film (at 650  $^\circ\text{C}$ ). The increase in the deposition rate during the gas-phase process and due to the higher deposition temperatures has been

**Fig. 2** XRD for Al–Ni coating film deposited at 650, 750, 850, and 950  $^\circ\text{C}$  by gas-phase hybrid deposition





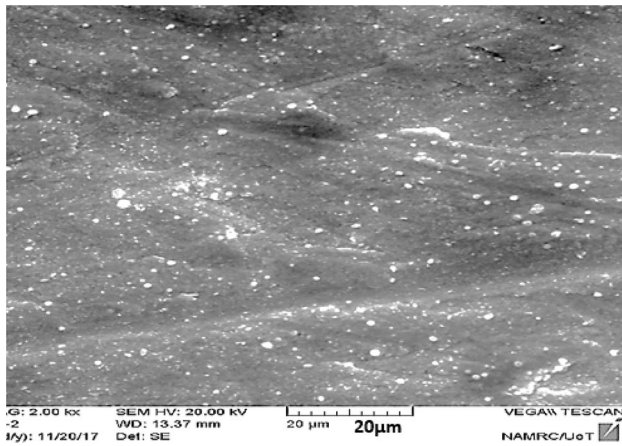


**Fig. 3** SEM topography for Al–Ni thin film at deposition temperature of 650 °C, with different magnifications

reported by other researchers as a result of the chemical reactions that took place during the deposition process; these chemical reactions will produce higher energy that will be delivered at higher deposition temperatures [11]. Since the formation of the coating layer in the gas-phase process is dominated by the occurrence of stable growth in the stable region of the phase diagram, accordingly, increasing substrate temperature will increase the energy of the growing film, leading to produce new phases in a crystalline form. With the higher deposition temperature, the XRD pattern for the Al–Ni coatings (at 850 °C) show new phases that were accrued by the chemical reactions between Al and Ni, where a composite coating phase of  $\text{Ni}_3\text{Al}$  (ICDD No. 00-050-1294) along with the Fe–Ni and the Al oxide phases can be observed in this pattern. At the higher deposition temperature (at 950 °C), the XRD pattern in Fig. 2 was noticed to be sharper with higher intensity and closer to the crystalline form of the Al–Ni films than the former patterns; this will result in an increase in the surface roughness along with the increase in the deposition temperature that is caused by the coarser Al–Ni phases

### 3.2 Surface morphology for gas-phase coatings

Figures 3, 4, 5, and 6 show the SEM surface morphology of Al–Ni coatings, which were deposited at deposition temperatures ranging from  $T_d = 650\text{--}950$  °C. From Fig. 3, the surface is characterized by the amorphous structures with thin microdroplets that represent the Fe–Ni and  $\text{Al}_2\text{O}_3$  compounds, since it is the only phase that was detected by XRD test for this sample, where the segregation has taken place due to the low deposition temperature used in this coating film. Also, the low deposition temperature resulted in low deposition rates that produce a very thin

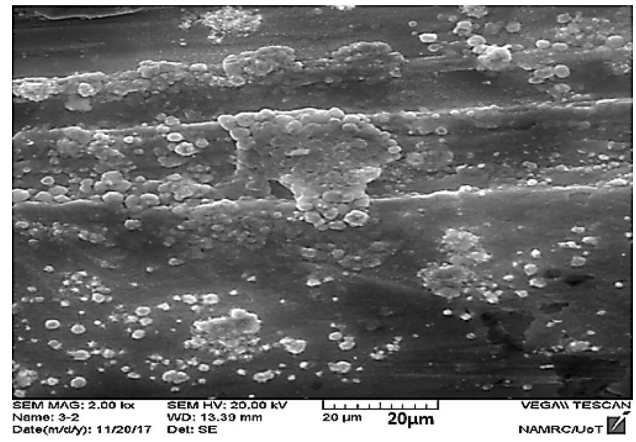


**Fig. 4** SEM topography for Al–Ni thin film at deposition temperature of 750 °C

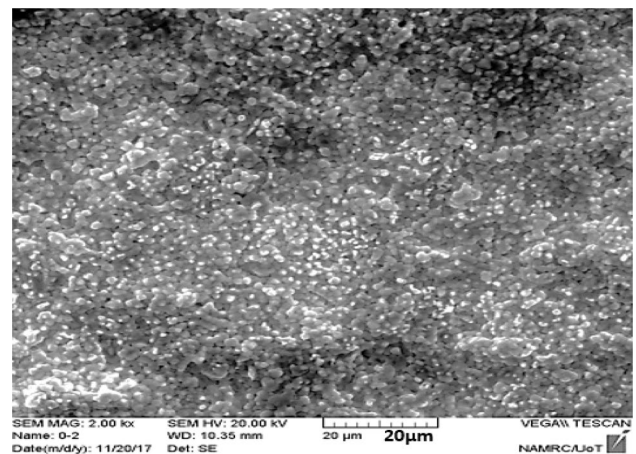


**Fig. 5** SEM topography for Al–Ni thin film at deposition temperature of 850 °C

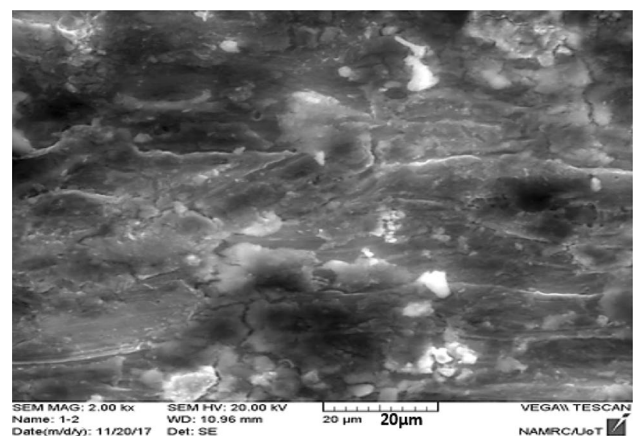


**Fig. 6** SEM topography for Al–Ni thin film at deposition temperature of 950 °C

coating film that can be easily identified from the very thin surface film that appears in this figure. Increasing the deposition temperature to 750 °C in Fig. 4 will result in a change in morphology toward a more crystalline structure. From the XRD tests, this was driven by the more crystalline phases that were formed in this deposition temperature (750 °C) and that finally lead to an increase in the average grain size as it can be noticed from the SEM images for this sample. This was also reported in the XRD test pattern for this sample. With further increase in the deposition temperatures to 850 °C, the coating surface in Fig. 5 was found to be denser but with higher surface roughness which resulted from the increase in the average grain size. Also, a globular and cubic shape structure, which was supported by the gas-phase deposition process and carried out in the air, was raised in these structures where the particles were not separated as there were many side connections. In Fig. 5, the narrowest size distribution and the finest particles that can be found in the ample that was produced at  $T_d = 850$  °C indicated that the formation of the coating layer was occurred due to the stable growth that took place in the stable region of the phase diagram for the Al–Ni system. The precipitates are presumed to be intermetallic phases of nickel and aluminum which formed as the result of the transformation phase of the coatings on the basis of the Ni–Al binary diagram [10]. Also, the globular mass transfer provided high deposition rates that can assist in the deposition of thick coatings but can result in a decrease in the crystallinity which is associated with an increase in the amorphous formed phases as it can be seen in Fig. 6 for Al–Ni coating that was deposited at  $T_d = 950$  °C.

### 3.3 Scratch test and optical microscopy observations

The scratch test was performed to determine the thin-film adhesion with the substrate by a diamond indenter that was drawn across the coated surface under a specific load; on the other hand, the test also aimed at estimating the cohesion between the coating and the substrate by the measurement of the scratch hardness, where the load is plotted as a function of the hardness of the substrate. Such test scratches were made by moving specimen under a vertically loaded indenter. During the scratch test, two distinct types of behavior can occur, depending on whether the observed failure is brittle or ductile. However, as it was reported by other researchers, some materials such as stainless steel can show both brittle and ductile behavior during scratch test depending on sample preparation [11]. This behavior is dominated by the existence of the oxide layer on the steel surface that can have an effect on the coating adhesion. For films deposited in this study, a ductile failure was observed, where the ductile failure

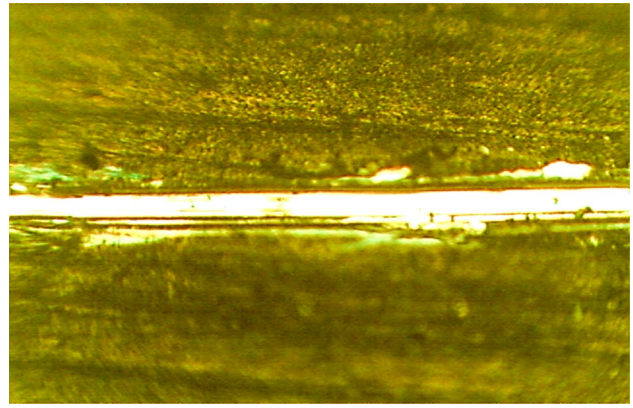


Fig. 7 Optical micrograph of the scratch in the Al–Ni coating at deposition temperature of 850 °C

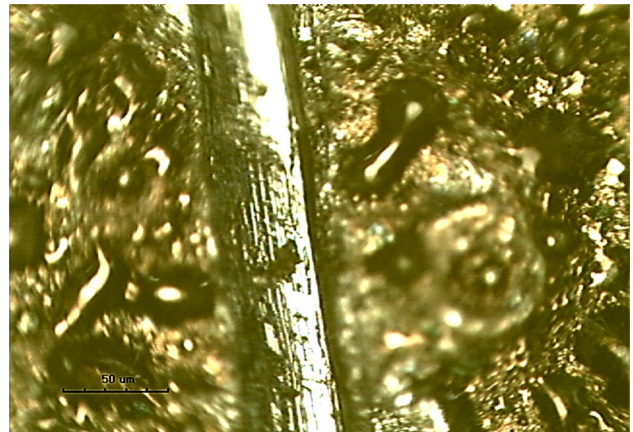


Fig. 8 Optical micrograph of the scratch in the Al–Ni coating at deposition temperature of 950 °C

is generally characterized by lower crack areas than the brittle failure and smaller chipped or spalled regions. Also, critical loads for ductile failure (exhibited by most metal substrates) are very much higher than those observed for brittle materials. As shown in Figs. 7 and 8, the microscopic images reveal that the failure tends to occur within the coating, which means that the adhesion is good.

The scratch hardness  $HS_L$  (Pa) was estimated following the specification of ASTM G171-03 norm:

$$HS_L = 8L/\pi d^2$$

where  $L$  (N) is the applied normal force (the load of 30 N was selected) and  $d$  (m) is the corresponding scratch width. The scratch hardness is an indicator of coating cohesion. The greater hardness was found for Al–Ni coating that was deposited at  $T_d = 950$  °C. This high hardness can be associated with stronger cohesion strength of the coating compared with the samples that were deposited



at lower temperatures. By the same way, low scratch hardness for samples deposited at  $T_d = 650$  and  $750$  °C was very small, which must result from the low deposition temperature and the low deposition rates as it was conducted in the SEM results.

The resulting coating thicknesses for the Al–Ni coatings at different deposition temperatures were determined from fracture cross-sectional samples that were examined by using optical microscopy. The results of the film thickness investigation indicate an increase in thickness along with the increase in the deposition temperatures, where the optical microscopy images in Fig. 9 show an increase in the thin-film thickness from 2 to 3  $\mu\text{m}$  for the samples that were deposited at low temperatures (650–750 °C), to higher thickness of 8–9  $\mu\text{m}$  for the sample that was produced at higher temperature (at 950 °C).

### 3.4 Electrochemical test for gas-phase coatings

Electrochemical tests were performed in order to evaluate the Al–Ni coating quality for corrosion resistance applications for the coated AISI 316 stainless steel that was tested under chloride containing electrolytes. The pitting corrosion resistance can be determined by the starting breakdown potential values during the electrochemical test, where many authors try to develop opinions for which breakdown potentials should be acceptable and which should be unacceptable for the stainless-steel alloys. The breakdown potential is termed as critical pitting potential when pitting is present [7, 12]. It was reported by many authors that for the more electronegative breakdown potential (more than +300 mV), the alloy is considered to not be in an optimal corrosion resistant condition [13, 14]. The cathodic and anodic polarization behavior

of the uncoated and the coated AISI 316 stainless-steel samples was recorded after 1 h exposure in 0.25 M hydrochloric acid (HCl). Their resistance to localized corrosion was investigated by electrochemical methods, including cyclic potentiodynamic polarization and potentiostatic polarization measurements (in Fig. 10) in an aqueous solution. Since the pitting potential and protection potential determined by potentiodynamic measurements depend not only on the material and electrolyte but also on the experimental procedure. In this procedure, the obtained values should be used with caution and not as intrinsic material parameters. The measured anodic polarization curve for the uncoated AISI 316S.S. is shown in Fig. 10. In this figure, the higher  $i_{\text{corr}}$  values and the shift of  $E_{\text{corr}}$  toward a more negative potential (Inters. Pot.: –174.0 mV, Inters. Cur.: 402.21 nA) could suggest an acceleration of the corrosion process; also, the re-passivation of an initiated localized attack will be difficult and corrosion will probably continue to propagate and cause undesirable chemical reactions or even failure of the metal. The Al–Ni coating that was applied on the stainless-steel surfaces reduced the current density of the surface within the limits of the anodic region, as it can be seen in Fig. 10, which leads to the conclusion that there is an improvement in corrosion resistance. Except for the case of samples that were deposited at 650 °C (that were not tested due to not uniform surface film); there is an improvement in corrosion resistance for all coated samples to a different extent. Where for the Al–Ni coating that was deposited at 750 °C, the pitting corrosion was observed after the test, which can probably be due to defects and the thin microdroplets presented in these samples (Inters. Pot.: –482.1 [mV] Inters. Cur.: 82.09  $\mu\text{A}$ ) that was caused by the low deposition rates due to the

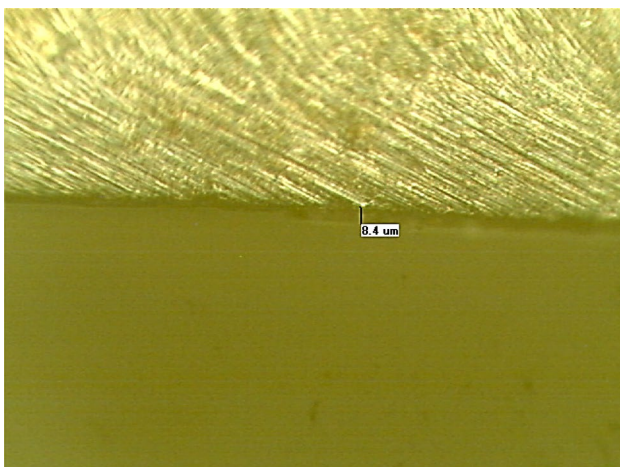


**Fig. 9** Fracture cross-sectional optical microscope image for coating thickness measurements

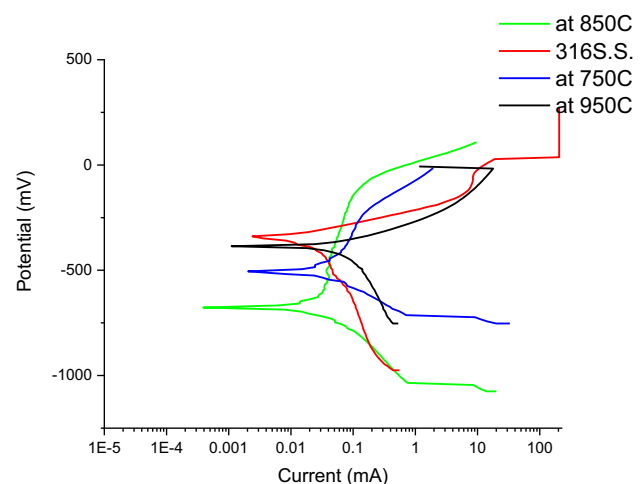


**Fig. 10** Measured anodic polarization curves by electrochemical test for the uncoated AISI316 St, and Al–Ni coating film deposited at 750,850, and 950 °C

low deposition temperature as it was indicated from the SEM and the XRD testes. For the other coating samples, the corrosion potential values of the composite layers are less negative than the one corresponding to the uncoated stainless steel, indicating that the Al–Ni coatings are less active than substrate surface. Moreover, the decreases in the corrosion current density in these samples compared to the i-corr value calculated for the uncoated surface could be associated to an increase in corrosion resistance of the composite coatings as a consequence of the formation of the passive film. In other words, the  $\text{Al}_2\text{O}_3$  and  $\text{Ni}_3\text{Al}$  phases presented on the coating surface that acted as uniform passive sites reduced the corrosion propensity of the coating. It should also be noted that no pitting corrosion was observed after the test in the coated surfaces that was deposited at 850, and 950 °C with Inters. Pot.: –495.1 [mV] Inters. Cur. 18.35  $\mu\text{A}$  for the Al–Ni coating that was deposited at 750 °C, and Inters. Pot.: –661.5 [mV] Inters. Cur. 11.94  $\mu\text{A}$ : for the Al–Ni coating that was deposited at 850 °C, and Inters. Pot.: –344.4 [mV] Inters. Cur. 7.19  $\mu\text{A}$  for the Al–Ni coating that was deposited at 950 °C, at potential test reached up to 2000 mV (i.e., no breakdown potential), where only general corrosion was generally observed.

## 4 Conclusion

A hybrid vapor deposition process (HDP) was successfully used to deposit Ni–Al composite coatings on the austenitic stainless-steels AISI 316 surface. It was very clear that the deposition rates and the produced coating phases in the coating film were affected by the deposition temperature, where higher deposition rate was obtained during the gas-phase process with increasing the deposition temperatures as a result of the chemical reactions that took place due to the higher energy that delivered at higher deposition temperatures. Also, with further increase in the deposition temperatures, the coating surface was found to be denser but with higher surface roughness which resulted from the increase in the average grain size. From the electrochemical test, except for the case of samples that were deposited at 750 °C, there is an improvement in corrosion resistance, which suggested that the corrosion potential values of the composite layers are less negative than the ones corresponding to the uncoated stainless steel, indicating that the Al–Ni coatings performed by HDP are less active in HCl environments than the substrate surface.

**Acknowledgement** The authors gratefully acknowledge the technical support provided by the Nanotechnology and Advanced Material Research Center, University of technology, Baghdad, Iraq.

## Compliance with ethical standards

**Conflict of interest** The authors declare that they have no conflict of interest.

## References

1. Klueh RL (2005) Properties and selection: irons, steels, and high performance alloys. In: ASM handbook, vol 1, Metals and Ceramics Division, Oak Ridge National Laboratory, pp 1384–1416
2. Thamer AD, Mohammed FQ, Hassan AS, Abid AL (2017) Corrosion resistance enhancement in acidic solution for austenitic stainless steel by gas-phase hybrid deposition process. *Eng Technol J* 35(Part A):788–794
3. Sánchez JG, Pérez LD, Ochoa EG, Canto G, Baz MS (2012) Corrosion pit growth on austenitic stainless steels in chloride containing solution: a quantitative approach. *Anti-Corros Methods Mater* 59(5):239–245
4. Mattox DM (1998) Handbook of physical vapor deposition (PVD) processing: film formation, adhesion, surface preparation and contamination control. Noyes Publications, Saddle River
5. Geng H (2004) Semiconductor manufacturing handbook. McGraw-Hill, New York
6. Helmersson U, Lattemann M, Böhlmark J, Ehiassarian AP, Gudmundsson JT (2006) Ionized physical vapor deposition (IPVD): a review of technology and applications. *Thin Solid Films* 513(1–2):1–24. <https://doi.org/10.1016/j.tsf.2006.03.033>
7. Stoloff NS, Rensselaer Polytechnic Institute, ASM handbook (2008) volume 1, properties and selection: irons, steels, and high performance alloys, elevated-temperature properties of stainless steels, pp 1443–1473
8. Thamer AD, Haider AJ, Mohammed FQ, Chahrour KM (2017) Hybrid gas phase Ti–B–C–N coatings doped with Al. *J Alloys Compd* 723:368–375
9. Rooy EL (2005) Introduction to aluminum and aluminum alloys. ASM international handbook vol. 2 nonferrous alloys and special-purpose materials. Aluminum Company of America, pp 17–39
10. Nash P, Singleton MF, Murray JL (2005) Binary alloy phase diagram. In: ASM international handbook (alloy phase diagrams), vol 3. pp 82–102
11. Jaworski R, Pawlowski L, Roudet F, Kozerski S, Petit F (2008) Characterization of mechanical properties of suspension plasma sprayed TiO<sub>2</sub> coatings using scratch test. *Surf Coat Technol* 202:2644–2653
12. Hawang GS, Moon SH (1999) Effect of surface kinetic on the step coverage during chemical vapor deposition. *J Mater Sci* 14:2377–2380
13. Sprowls DO (2005) Evaluation of pitting corrosion. In: ASM handbook, vol 13, corrosion. pp 516–520
14. Protopopoff E, Marcus P (2003) Potential measurements with reference electrodes, corrosion: fundamentals, testing, and protection, vol 13A. ASM Handbook, ASM International, pp 13–16

**Publisher's Note** Springer Nature remains neutral with regard to jurisdictional claims in published maps and institutional affiliations.